

# Dynamical Cluster Approximation Employing FLEX as a Cluster Solver

K. Aryanpour<sup>1</sup>, M. H. Hettler<sup>2</sup> and M. Jarrell<sup>1</sup>

<sup>1</sup>*University of Cincinnati, Cincinnati OH 45221, USA*

<sup>2</sup>*Forschungszentrum Karlsruhe, Institut für Nanotechnologie, Karlsruhe, Germany*

We employ the Dynamical Cluster Approximation (DCA) in conjunction with the Fluctuation Exchange Approximation (FLEX) to study the Hubbard model. The DCA is a technique to systematically restore the momentum conservation at the internal vertices of Feynman diagrams relinquished in the Dynamical Mean Field Approximation (DMFA). FLEX is a perturbative diagrammatic approach in which classes of Feynman diagrams are summed over analytically using geometric series. The FLEX is used as a tool to investigate the complementarity of the DCA and the finite size lattice technique with periodic boundary conditions by comparing their results for the Hubbard model. We also study the microscopic theory underlying the DCA in terms of compact (skeletal) and non-compact diagrammatic contributions to the thermodynamic potential independent of a specific model. The significant advantages of the DCA implementation in momentum space suggests the development of the same formalism for the frequency space. However, we show that such a formalism for the Matsubara frequencies at finite temperatures leads to acausal results and is not viable. However, a real frequency approach is shown to be feasible.

## I. INTRODUCTION

Non-local correlations play an important role in the physics of strongly correlated electron systems such as high- $T_c$  superconductors, heavy fermion metals, etc. The Dynamical Mean Field Approximation (DMFA) [1,2], in which all the non-local correlations are ignored, can capture some of the major features of strongly correlated systems. Nevertheless, the non-local correlations become crucial in the physics of phases with non-local order parameters such as d-wave superconductivity. Even phases with local order parameters such as commensurate magnetism can be significantly affected by the non-local correlations (e.g. spin waves) ignored in the DMFA.

The early attempts to extend the DMFA by including non-local correlations resulted in the violation of causality which is a requirement for positive definiteness of the spectral weight and the density of states (DOS) [3]. The Dynamical Cluster Approximation (DCA) is a fully causal technique used to systematically add nonlocal corrections to the DMFA by mapping the lattice onto a self-consistently embedded cluster problem. The mapping from the lattice to the cluster is accompanied by coarse-graining the lattice problem in its reciprocal space. Thus far, the DCA has been combined with Quantum Monte Carlo (QMC) [4,5], the Non-Crossing Approximation (NCA) [6] and the Fluctuation Exchange Approximation (FLEX) [11,12] to solve the corresponding cluster

problems.

The FLEX is a perturbative diagrammatic approach in which classes of Feynman diagrams are summed to all orders using geometric series. [7,8] Others [9,10] have employed the FLEX for finite size lattices with periodic boundary conditions. Due to the absence of contributions from some relevant diagrams, the FLEX is not capable of addressing the Hubbard model physics in the strong regime precisely. However, the main objective of this work is to make a comparison between the DCA-FLEX combination results and previous finite size lattice FLEX calculations. It is hoped that this study will lead to a better understanding of the DCA.

We earlier [11] suggested a prescription to correctly implement the DCA technique in the thermodynamic potential. This prescription will be discussed from a different point of view using a more general argument. Based upon the Green function's exponential fall-off as a function of distance, we conclude that compact diagrams (two-particle irreducible in the thermodynamic potential) are better approximated using the DCA than non-compact (two-particle reducible) ones. Hence, the DCA is applied to the compact diagrams only and non-compact ones are calculated explicitly using dressed non coarse-grained Green functions.

In this work we also consider the extension of the DCA to frequency space. The many-body theory at finite temperatures is conventionally derived in terms of discrete imaginary Matsubara frequencies. We illustrate that even for a self-consistent algorithm like the FLEX, coarse-graining the imaginary frequency propagators results in causality violations and can not be implemented. However, a real frequency formalism is shown to be causal and applicable not only to the FLEX, but also to other cluster solving methods such as the NCA.

This paper is structured as follows. In the next three sections, we briefly review the DCA, its application to the Hubbard model, the FLEX, and then we describe how the FLEX and the DCA may be merged into a single algorithm. In the next three sections, we use the FLEX-DCA, in comparison to the FLEX for finite-sized systems, to explore the properties of the DCA. The last two sections, are devoted to a microscopic derivation of the DCA, and to an extension of the DCA to frequency space.

## II. DYNAMICAL CLUSTER APPROXIMATION (DCA)

Both the DCA and the DMFA may be derived by exploring the momentum conservation in the diagrammatics. As depicted in Fig. 1, momentum conservation at each vertex is described by the Laue function:

$$\Delta = \sum_{\mathbf{x}} e^{i\mathbf{x} \cdot (\mathbf{k}_1 - \mathbf{q} - \mathbf{k}_2)} = N \delta_{\mathbf{k}_1, \mathbf{q} + \mathbf{k}_2}, \quad (1)$$

In the DMFA, momentum conservation at the internal vertices of irreducible Feynman diagrams is completely relinquished. I.e., the DMFA simply sets  $\Delta = 1$ . [13] Hence, we may sum freely over all the internal momenta entering and leaving each vertex. Only local contributions survive the sum. Thus, this is equivalent to mapping the lattice problem onto a self-consistently embedded impurity problem. The DMFA becomes exact at infinite dimensions. [14]

The DCA is an approach to systematically restore the momentum conservation relinquished in the DMFA. In the DCA, the first Brillouin zone in the reciprocal space is divided into  $N_c$  equal cells of linear size  $\Delta k$  labeled by  $\mathbf{K}$  in their centers, and the momenta within each cell are labeled by  $\tilde{\mathbf{k}}$ . Then  $\mathbf{k} = \mathbf{K} + \tilde{\mathbf{k}}$  (c.f. Fig. 2). To visualize this scheme in the real lattice, one could consider tiling the lattice of  $N$  sites by  $N/N_c$  clusters each composed of  $N_c = L^D$  sites where  $L$  is the linear size of the subcell and  $D$  is dimensionality (c.f. Fig. 2 for  $L = 2$ ). We will use this picture in section VIII while discussing the microscopic theory of the DCA. We label the origin of the clusters by  $\tilde{\mathbf{x}}$  and the  $N_c$  intercluster sites by  $\mathbf{X}$ . So for each site in the original lattice  $\mathbf{x} = \mathbf{X} + \tilde{\mathbf{x}}$ . Care must be taken when choosing the cluster geometries in order to preserve the lattice point group symmetry and also satisfy some other criteria for cubic or square lattices. [15]

In the DCA, we first make the following separation in Eq. 1

$$\Delta = \sum_{\mathbf{x}} e^{i(\tilde{\mathbf{x}} + \mathbf{X}) \cdot (\mathbf{K}_1 - \mathbf{Q} - \mathbf{K}_2 + \tilde{\mathbf{k}}_1 - \tilde{\mathbf{q}} - \tilde{\mathbf{k}}_2)}. \quad (2)$$

The products  $\mathbf{K}_1 \cdot \tilde{\mathbf{x}}$ ,  $\mathbf{Q} \cdot \tilde{\mathbf{x}}$  and  $\mathbf{K}_2 \cdot \tilde{\mathbf{x}} = 2n\pi$  where  $n$  is an integer. Therefore, their associated phases may be neglected and Eq. 1 splits into two parts

$$\Delta = \frac{N}{N_c} \delta_{\tilde{\mathbf{k}}_1, \tilde{\mathbf{q}} + \tilde{\mathbf{k}}_2} N_c \delta_{\mathbf{K}_1, \mathbf{Q} + \mathbf{K}_2}. \quad (3)$$

The DCA also ignores the phases  $e^{-i\tilde{\mathbf{k}} \cdot \tilde{\mathbf{x}}}$  due to the position of the cluster in the original lattice and (far less important)  $e^{-i\tilde{\mathbf{k}} \cdot \mathbf{X}}$  corresponding to the position within the cluster. As a result, it approximates  $N/N_c \delta_{\tilde{\mathbf{k}}_1, \tilde{\mathbf{q}} + \tilde{\mathbf{k}}_2} \cong 1$ , so that

$$\Delta_{DCA} = N_c \delta_{\mathbf{K}_1, \mathbf{Q} + \mathbf{K}_2}, \quad (4)$$

which indicates that the momentum is conserved modulo  $\Delta k$  for transfers between the cells.

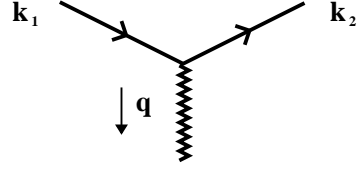


FIG. 1. A typical vertex in a Feynman diagram with solid lines as one particle Green functions and the wiggly line as an interaction.

The approximation made through the substitution  $\Delta \rightarrow \Delta_{DCA}$  corresponds to replacing all internal legs in the compact (skeletal) diagrams by the coarse-grained Green function  $\bar{G}$  and interaction potential  $\bar{V}$  defined by

$$\bar{G}(\mathbf{K}, \omega_n) = \frac{N_c}{N} \sum_{\tilde{\mathbf{k}}} G(\mathbf{K} + \tilde{\mathbf{k}}, \omega_n), \quad (5)$$

$$\bar{V}(\mathbf{Q}) = \frac{N_c}{N} \sum_{\tilde{\mathbf{q}}} V(\mathbf{Q} + \tilde{\mathbf{q}}). \quad (6)$$

In section VIII, we will define the compact and non compact diagrams and elaborately discuss why only the compact ones undergo the coarse-graining approximation.

Replacing  $\Delta$  by  $\Delta_{DCA}$  tremendously reduces the complexity of the problem because instead of having to perform sums over all  $N$  states in the entire first Brillouin zone, we have sums over only a set of  $N_c$  states where  $N_c \ll N$ .

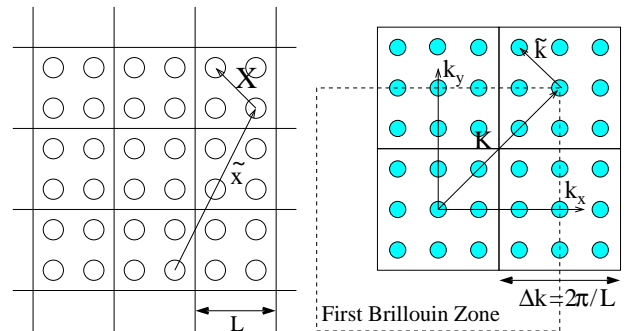


FIG. 2. The real lattice clusters (right) and (left) the first Brillouin zone divided into subcells.

## III. HUBBARD MODEL

We will apply the DCA to study the Hubbard model Hamiltonian incorporating interactions between the electrons on a lattice. It includes a tight-binding part due to the hopping of electrons among the sites and an interaction between the electrons. The general Hamiltonian reads

$$H = H_0 + H_I, \quad (7)$$

where

$$H_0 = -t \sum_{\sigma} \sum_{\langle ij \rangle} c_{i\sigma}^\dagger c_{j\sigma}, \quad (8)$$

and

$$H_I = \frac{1}{2} \sum_{jl, \sigma\sigma'} n_{j\sigma} n_{l\sigma'} V(R_j - R_l) \\ V(R) \approx \frac{e^2}{R}. \quad (9)$$

Factors  $t$  and  $V(R)$  correspond to electron hoppings and Coulomb interactions respectively. Later in the paper, we will study the simplest Hubbard interaction which is fully local and only between electrons sitting at the same site having opposite spin directions. The interaction strength is a constant called  $U$ . Hence, for the local model, Eq. 9 simplifies to

$$H_I = U \sum_i n_{i\uparrow} n_{i\downarrow}. \quad (10)$$

In terms of the vertex properties addressed in section II, since the interaction is local and therefore independent of  $\mathbf{q}$ , we may sum freely over the  $\mathbf{q}$  momentum for a pair of Laue functions in Eq. 1 sharing a common interaction wiggly line as depicted in Fig. 1. As a result, the corresponding Laue function will become

$$\Delta = \frac{1}{N} \sum_{\mathbf{q}} \sum_{\mathbf{x}} e^{i\mathbf{x} \cdot (\mathbf{k}_1 - \mathbf{q} - \mathbf{k}_2)} \sum_{\mathbf{y}} e^{i\mathbf{y} \cdot (\mathbf{k}_3 + \mathbf{q} - \mathbf{k}_4)} = \\ N \sum_{\mathbf{q}} \delta_{\mathbf{k}_1, \mathbf{q} + \mathbf{k}_2} \delta_{\mathbf{k}_3 + \mathbf{q}, \mathbf{k}_4} = N \delta_{\mathbf{k}_1 + \mathbf{k}_3, \mathbf{k}_2 + \mathbf{k}_4}, \quad (11)$$

and analogously for the DCA, by summing freely over  $\mathbf{Q}$

$$\Delta_{DCA} = N_c \delta_{\mathbf{K}_1 + \mathbf{K}_3, \mathbf{K}_2 + \mathbf{K}_4}. \quad (12)$$

#### IV. FLUCTUATION EXCHANGE APPROXIMATION (FLEX)

In the Feynman diagrammatics of the Hubbard model with a local interaction, all the interactions (wiggly lines in Fig. 3) contribute a c-number  $U$  from Eq. 10. The electronic Green functions (solid lines) which interact with one another should have opposite spins. Considering these restrictions, had we been able to include all the possible diagrams in our expansion we would have solved the problem exactly. However, in practice this is not feasible.

The Fluctuation Exchange Approximation (FLEX) was introduced as an approximate technique to simplify this diagrammatic sum [7,8], while retaining a conserving

approximation. In the FLEX, the interaction part of the Hubbard model Hamiltonian is treated perturbatively by selecting a certain class of all the possible diagrams which may be summed as a geometric series. Following Baym [16], we define the generating functional  $\Phi[G(k, \omega_n)]$  as the collection of all the selected families of diagrams illustrated in Fig. 3. Therefore,  $\Phi[G(k, \omega_n)]$  for the FLEX can be written

$$\Phi = \Phi_{ph}^{df} + \Phi_{ph}^{sf} + \Phi_{pp}, \quad (13)$$

$$\Phi_{ph}^{df} = -\frac{1}{2} \text{Tr} [\chi_{ph}]^2 + \frac{1}{2} \text{Tr} [\ln(1 + \chi_{ph}) - \chi_{ph} + \frac{1}{2} \chi_{ph}^2], \quad (14)$$

$$\Phi_{ph}^{sf} = \frac{3}{2} \text{Tr} [\ln(1 - \chi_{ph}) + \chi_{ph} + \frac{1}{2} \chi_{ph}^2], \quad (15)$$

$$\Phi_{pp} = \text{Tr} [\ln(1 + \chi_{pp}) - \chi_{pp} + \frac{1}{2} \chi_{pp}^2], \quad (16)$$

where  $\text{Tr} = (T/N) \sum_k \sum_n$  with  $T$  the temperature and  $N$  the number of lattice sites. The particle-hole and particle-particle susceptibility bubbles are

$$\chi_{pp}(q, \omega_n) =$$

$$U(T/N) \sum_k \sum_m G(k + q, \omega_n + \omega_m) G(-k, -\omega_m), \quad (17)$$

$$\chi_{ph}(q, \omega_n) =$$

$$-U(T/N) \sum_k \sum_m G(k + q, \omega_n + \omega_m) G(k, \omega_m), \quad (18)$$

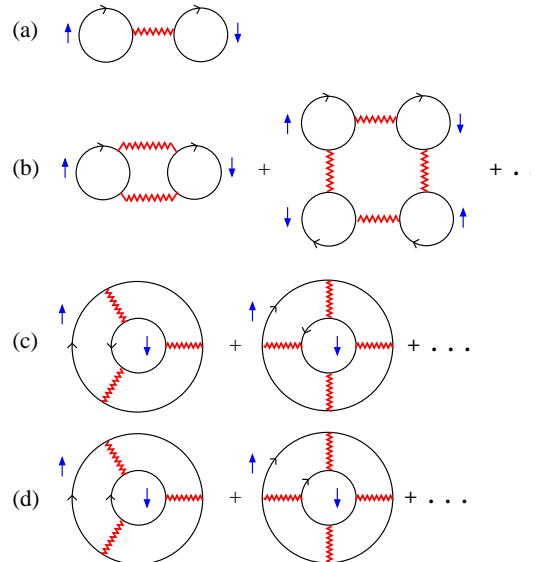


FIG. 3. (a) Lowest order diagram (Hartree term), (b) longitudinal spin and density fluctuation  $\Phi$  diagrams with an even number of bubbles ( $\Phi_{ph}^{df}$ ), (c) transverse spin fluctuations ( $\Phi_{ph}^{sf}$ ) and (d) particle-particle fluctuations ( $\Phi_{pp}$ ).

The self-energy and the Green function are defined by

$$\Sigma(k, \omega_n) = \frac{1}{2} \frac{\delta \Phi[G]}{\delta G(k, \omega_n)}, \quad (19)$$

$$G(k, \omega_n) = [G^{(0)-1}(k, \omega_n) - \Sigma(k, \omega_n)]^{-1}, \quad (20)$$

where  $G^{(0)}$  is the non-interacting one particle Green function defined by

$$G^{(0)}(\mathbf{k}, \omega_n) = \frac{1}{\omega_n - \epsilon_{\mathbf{k}} + \mu}, \quad (21)$$

with  $\epsilon_{\mathbf{k}}$  the non-interacting Hubbard model dispersion and  $\mu$  the chemical potential.

Calculating the self-energy for Eq. 13 using Eq. 19 we get

$$\begin{aligned} \Sigma(k, \omega_n) = U(T/N) \sum_q \sum_m & [V^{(ph)}(q, \omega_m) \times \\ & G(k - q, \omega_n - \omega_m) - V^{(pp)}(q, \omega_m) \times \\ & G(-k + q, -\omega_n + \omega_m)], \end{aligned} \quad (22)$$

in which

$$\begin{aligned} V^{(ph)}(q, \omega_m) = \chi_{ph}(q, \omega_m) + \frac{1}{2} \chi_{ph}(q, \omega_m) \times \\ \left[ \frac{1}{1 + \chi_{ph}(q, \omega_m)} - 1 \right] + \frac{3}{2} \chi_{ph}(q, \omega_m) \times \\ \left[ \frac{1}{1 - \chi_{ph}(q, \omega_m)} - 1 \right], \end{aligned} \quad (23)$$

$$V^{(pp)}(q, \omega_m) = \chi_{pp}(q, \omega_m) \left[ \frac{1}{1 + \chi_{pp}(q, \omega_m)} - 1 \right]. \quad (24)$$

Eq. 23,24 for the potential functions  $V^{(ph)}$  and  $V^{(pp)}$  are geometric series for  $\chi_{ph}$  and  $\chi_{pp}$  similar to the *random phase approximation* (RPA) results. The Hartree term contribution to the self-energy has not explicitly appeared in Eq. 22 as it is constant and can be always embedded in the chemical potential in Eq. 21.

The difference  $\Delta\Omega(T, \mu)$  between interacting and non-interacting thermodynamic potential functional is also expressible in terms of the Green functions, self-energy, and  $\Phi[G]$

$$\Delta\Omega(T, \mu) = \Omega - \Omega_0 = -2\text{Tr}[\Sigma G - \ln(G/G_0)] + \Phi[G]. \quad (25)$$

In the FLEX, since we include only a limited set of all the diagrammatic contributions, we do not anticipate to precisely address the Hubbard model physics. However, there are a number of significant physical features such as anti-ferromagnetic order at half filling and low temperatures that this approximation is able to capture. Moreover, by using the FLEX both together with the DCA

and to study finite sized systems with periodic boundary conditions, we can study the differences between these approaches. For example, as we will shortly illustrate, the complementarity of the DCA and finite size lattice techniques is manifest in the FLEX. The FLEX can also be invoked as a good test for the microscopic theory of the DCA and the coarse-graining effects in the compact and non-compact diagrams for Eq. 25.

## V. THE COMBINATION OF THE FLEX AND DCA (ALGORITHM)

In the combination of the FLEX and DCA, our goal is to calculate the self-energy in Eq. 19 whereby we construct the dressed Green function for the lattice as a building block for all the relevant physical quantities. We start out with the bare (non-interacting) Green function  $G^{(0)}(\mathbf{k}, z)$  defined in Eq. 21 with  $z$  the Matsubara frequency (complex). We coarse-grain  $G$  as directed in Eq. 5 and calculate the self-energy using Eq. 19. This is used to recompute the dressed Green function

$$G(\mathbf{k}, z) = \frac{1}{z - \epsilon_{\mathbf{k}} + \mu - \Sigma_{DCA}(\mathbf{K}, z)}. \quad (26)$$

where the index DCA in  $\Sigma_{DCA}(\mathbf{K}, z)$  indicates that we have used coarse-grained  $\bar{G}$  for the construction of self-energy. The new  $G$  is coarse-grained and used to calculate a new estimate of  $\Sigma_{DCA}(\mathbf{K}, z)$ . We repeat this process iteratively until convergence at a desired tolerance is obtained. The final self-energy is used to construct the dressed Green function in Eq. 26, required to compute the physical quantities such as spectral function, the density of states (DOS), etc. The algorithm of this calculation is demonstrated in Fig 4.

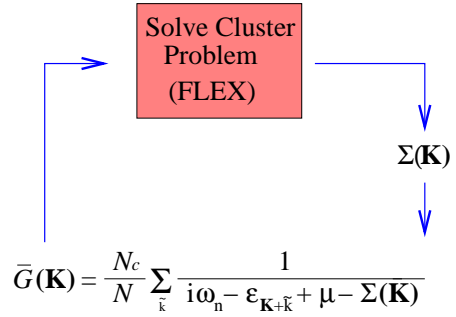


FIG. 4. The FLEX-DCA numerical algorithm. The dressed  $G$  is solved self-consistently with  $\Sigma$ . The iteration process stops whenever convergence is achieved.

## VI. COMPLEMENTARITY OF THE DCA TO THE FINITE SIZE LATTICE APPROXIMATION WITH PERIODIC BOUNDARY CONDITIONS

In the half-filled Hubbard model, the antiferromagnetic correlation length  $\xi$  increases with decreasing tempera-

ture and diverges at the phase transition. In a finite size lattice with periodic boundary conditions, as the temperature drops, once the correlation length reaches the size of the lattice, the system is fully frozen and there is a gap to excitations (c.f. Fig 5.a). In contrast, in the DCA, the correlations are confined within clusters of size  $N_c \ll N$  (the size of the entire lattice) and they never reach the size of the lattice. As we lower the temperature, the correlation length approaches the size of the cluster but since the lattice remains in the thermodynamic limit, it never freezes (c.f. Fig 5.b). By increasing the size of clusters in the DCA, we take longer ranged correlations into account so the gap will become more pronounced. Consequently, correlation induced gaps are generally overestimated in the finite size lattice, while in the DCA they are underestimated.

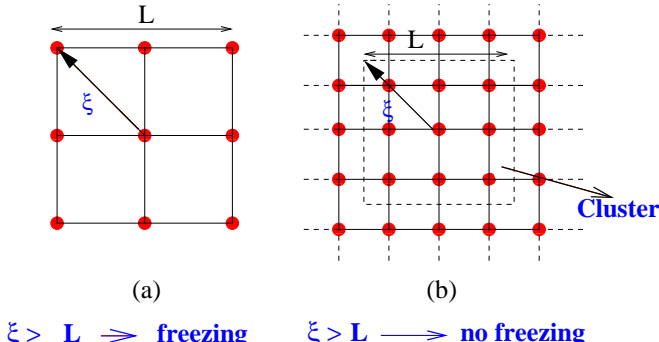


FIG. 5. (a) The finite size lattice with periodic boundary conditions, size  $L$  and correlation length  $\xi$  and (b) the lattice with clusters of size  $L$  and the correlation length  $\xi$ .

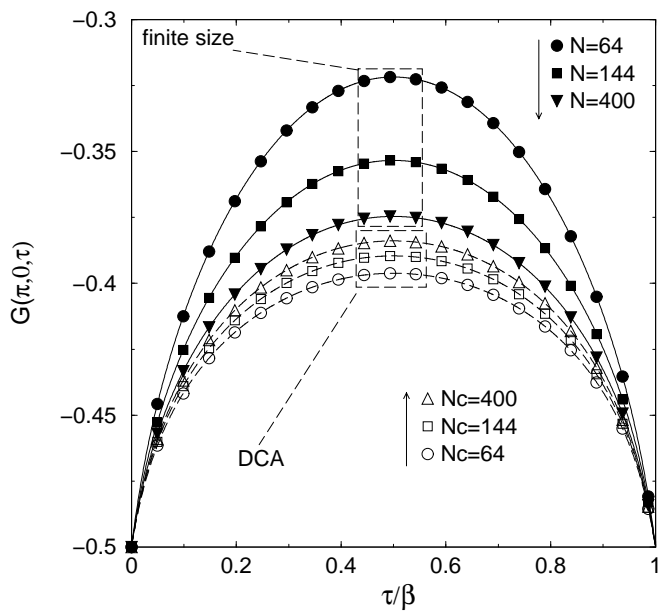


FIG. 6. The Green function  $G(k = (0, \pi), \tau)$  at  $T = 0.10$  and  $U/t = 1.57$  versus imaginary time  $\tau/\beta$  ( $\beta = 1/T$ ). Finite size results (filled symbols) and DCA results (open symbols) are displayed for lattice sizes of  $N = 8 \times 8$ ,  $12 \times 12$ , and  $20 \times 20$ . The curves show the complementary approach of the two methods to the thermodynamic limit.

This complementary behavior may be seen in  $G(k, \tau)$ , with  $k = (0, \pi)$  computed using finite size lattices with periodic boundary conditions and the DCA. As illustrated in Fig. 6, by increasing the size of the finite size lattice and the DCA cluster, the Green functions converge from opposite directions. In the finite size lattice, the Green function (e.g. at  $\tau = \beta/2$ ) decreases with the increase of size which is consistent with overestimating the gap; while in the DCA, the Green function increases as the cluster size grows consistent with underestimating the gap. It is also observed that the convergence in the DCA is much faster, meaning that the result of the DCA is closer to the true curve at a given cluster size. Both finite size lattices with periodic boundary conditions and the DCA converge with corrections of  $\mathcal{O}(\lambda/L^2)$  with  $L$  the linear size of the finite lattice or the DCA cluster and  $\lambda$  a coefficient. [17] The faster convergence of the DCA corresponds to its smaller  $\lambda$  compared to finite size lattices.

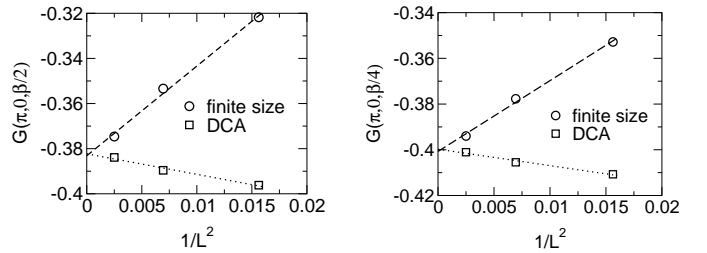


FIG. 7. The Green function  $G(k = (0, \pi), \tau)$  at  $\tau = \beta/2$  (left) and  $\tau = \beta/4$  (right) versus  $1/L^2$  for the DCA and finite size results in Fig. 6. The linear extrapolations meet at a point representing the thermodynamic limit of the Green function of the Hubbard model evaluated within FLEX.

In Fig. 7, the values of the  $G(k = (0, \pi), \tau = \beta/2)$  and  $G(k = (0, \pi), \tau = \beta/4)$  in Fig. 6 have been plotted versus  $1/L^2$  for both the DCA and finite size results. The Green function behaves linearly as a function of  $1/L^2$  for large  $L$ . The extrapolations of the DCA and finite size results meet as  $L \rightarrow \infty$ , approximating the value of the dressed Green function in the thermodynamic limit. The complementarity of DCA and finite size methods allows a determination of the thermodynamic limit of imaginary time Green functions with unprecedented accuracy.

## VII. FINITE SIZE VERSUS THE DCA FLEX RESULTS FOR THE TWO DIMENSIONAL HUBBARD MODEL AT HALF-FILLING

The Hubbard model at half filling undergoes a phase transition to anti-ferromagnetic order at low temperatures. According to the Mermin-Wagner-Hohenberg theorem, for dimension  $D = 2$  the critical temperature is zero. However, as we continue to lower the temperature, close enough to zero, a pseudogap will appear in the density of states (DOS) as a precursor to the anti-ferromagnetic phase (which has a full gap as its signature). An approach towards non-Fermi-liquid behavior is also visible in both the real and imaginary parts of the retarded self-energy. [9]

In Fig. 8 and Fig. 9, the densities of states (DOS) for lattices with finite sizes of  $32 \times 32$ ,  $64 \times 64$  and periodic boundary conditions and coarse-graining cluster sizes of  $16 \times 16$  and  $32 \times 32$  are plotted. We analytically continue the Green function in order to calculate the spectral function  $A(k, \omega)$  and DOS using the Padé approximation. [18] In this approximation, we generate a continued fraction interpolating all the data points and use it as an analytic function of the Matsubara frequencies  $\omega_n$ . The analytic continuation is accomplished by substituting  $\omega_n$  with  $\omega + i\eta$  where  $\eta$  is a small positive shift. However, the errors inherent in the numerical Fourier transform (FFT) and also the sharp high-frequency behavior of the Green function, FLEX potentials and the self-energy, limit the accuracy of the Padé. The high-frequency behavior is improved by implementing a more authentic cut off scheme introduced by Deisz *et al.* [19] in which the high-frequency tails of these quantities are Fourier transformed analytically prior to any numerical FFT and added back to the FFT outputs afterwards. In addition to this high-frequency cut off improvement, we also check for the analyticity of the Padé results in the upper-half frequency plane as a requirement for retarded physical quantities. This task is carried out by converting the continued fraction in the Padé into a ratio of two polynomials. The complex roots of these two polynomials are obtained via the Jenkins-Traub root finder routine. [20] Those orders of the Padé for which there exist poles in the upper-half plane are omitted unless these poles are canceled by the roots of the numerator. The acceptable Padé results correspond to the highest order with no uncompensated poles in the upper-half plane.

As seen in Fig. 8, by increasing the size of a finite lattice, the pseudogap occurs at higher temperatures and it also becomes less pronounced (sharper) as we approach the actual size of an infinite real lattice. The DCA yields a complementary behavior as shown in Fig. 9. By increasing the coarse-graining cluster size, similar to the finite size lattices, the pseudogap is shifted towards higher temperatures. However, unlike the finite size lattices, for the DCA the precursor becomes more pronounced (broader) as the cluster increases in size because the size

of the lattice remains constant and the correlations are limited to the cluster size. Thus comparatively, the DCA underestimates the gap while the finite size calculation overestimates it.

By comparing the results in Fig. 8 and Fig. 9 one may see that the  $32 \times 32$  DCA cluster yields more realistic physics than the corresponding  $32 \times 32$  finite size lattice. The  $64 \times 64$  finite size lattice results are also close to those for the  $32 \times 32$  DCA cluster at slightly lower  $T$  (eg,  $T = 0.055$  for the finite size and  $T = 0.033$  for the DCA). However since the sizes of clusters are considerably smaller than the sizes of lattices, the DCA significantly reduces the complexity of the problem and consequently the CPU time. In terms of the CPU time, the FLEX with the numerical Fourier transforms scales as  $\mathcal{N} \ln \mathcal{N}$  where  $\mathcal{N}$  is the product of the total number of Matsubara frequencies and the  $k$  points in the first Brillouin zone. Hence, using a  $32 \times 32$  cluster in place of a  $64 \times 64$  lattice both having 1024 Matsubara frequency points roughly reduces the CPU time by a factor of 4.4. If the DCA cluster size  $N_c$  equals the size of the finite lattice  $N$ , the DCA requires somewhat more CPU time than the finite size lattice due to coarse-graining. Nevertheless, comparatively, for large finite lattices such as  $64 \times 64$ , the lattice size contributions to the CPU time significantly dominate the coarse-graining ones in a  $32 \times 32$  cluster. Thus, the  $32 \times 32$  DCA cluster is much faster.

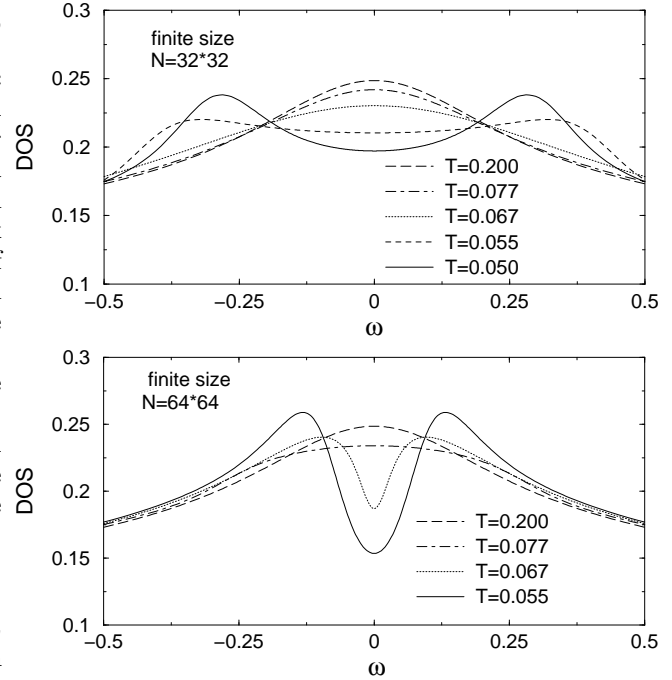


FIG. 8. The FLEX density of states (DOS) for a  $32 \times 32$  finite size lattice with periodic boundary conditions (top) versus energy for  $U/t = 1.57$  at various temperatures, and for a  $64 \times 64$  finite size lattice (bottom). The evolution of a weak pseudogap is observed at  $T = 0.067$  for the  $64 \times 64$  lattice higher than  $T = 0.055$  for the  $32 \times 32$  one and the pseudogap is also much broader for the  $32 \times 32$  lattice ( $128 \times 128$  finite size lattice results were obtained by Deisz *et al.* [9]).

The FLEX often has difficulty reaching low temperatures. This is due to the fact that the  $\chi_{ph}$  defined in Eq. 18 approaches unity as the temperature drops which in turn causes the  $V^{(ph)}$  in Eq. 23 to diverge. In the DCA,  $\chi_{ph}$  approaches unity more slowly, allowing the calculations to reach lower temperatures. One has to note that in the FLEX, the  $\chi_{ph}^{DCA}$  is defined as follows

$$\chi_{ph}^{DCA}(\mathbf{Q}, \omega_n) = -U(T/N_c) \sum_{\mathbf{K}} \sum_m \bar{G}(\mathbf{K} + \mathbf{Q}, \omega_n + \omega_m) \bar{G}(\mathbf{K}, \omega_m), \quad (27)$$

with  $\bar{G}$  defined in Eq. 5. Fig. 10 illustrates the saturation of  $\chi_{ph}$  for both the DCA and finite size lattices. The  $\chi_{ph}$  for the  $32 \times 32$  finite size lattice (filled circles) saturates at higher temperatures compared to the  $32 \times 32$  DCA cluster (open diamonds) indicating that in the DCA, for a certain cluster size, the precursor to the phase transition can evolve to lower temperatures compared to a finite size lattice of the same size with periodic boundary conditions. However, for the correlation length  $\xi > L$  the DCA approximation breaks down and replacing the self-energy by its coarse-grained counterpart is no longer accurate. Here, the DCA takes on significant mean-field character.

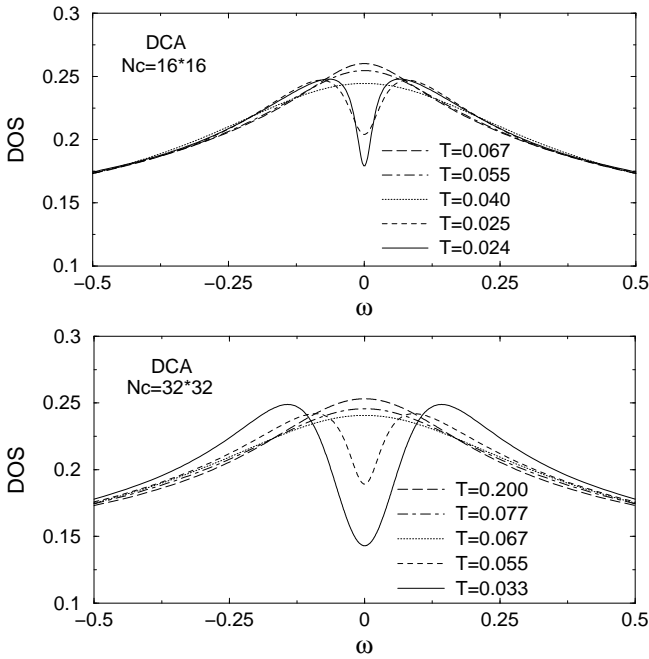


FIG. 9. The FLEX density of states (DOS) for a  $16 \times 16$  DCA cluster (top) versus energy for  $U/t = 1.57$  at various temperatures, and for a  $32 \times 32$  DCA cluster (bottom). For the  $32 \times 32$  cluster, the evolution of a weak pseudogap is observed at  $T = 0.055$  higher than  $T = 0.025$  for the  $16 \times 16$  one and the pseudogap is also broader for the  $32 \times 32$  cluster.

Another feature of the Hubbard model near half-filling verified by the FLEX [9] is non-Fermi-liquid behavior. Here, this is studied by increasing the electron-electron interaction  $U$  at a constant temperature. In Fig. 11 and Fig. 12 the real and imaginary parts of the self-energy at the  $X$  point (on the non-interacting Fermi surface) have been plotted versus energy for finite size lattices and the DCA respectively. As the interaction is increased, the negative slope in the real part turns positive around  $\omega = 0$  which is inconsistent with the requirement that the renormalization factor  $[1 - \partial \text{Re}\Sigma(\mathbf{k}_F, \omega)/\partial \omega|_{\omega=0}]^{-1}$  should be smaller than unity in the Fermi-liquid theory. There also appears an anomalous inverted peak in the imaginary part at  $\omega = 0$ .

As presented in Fig. 11, by increasing the length of the finite size lattice, the sharpness of the non-Fermi-liquid features is reduced. The same features for the DCA in Fig. 12 are slightly less pronounced and in a complementary fashion to the finite size lattices, their sharpness is enhanced by increasing the size of the cluster. Thus, again the DCA underestimates the non-Fermi-liquid features while the finite size calculation overestimates it.

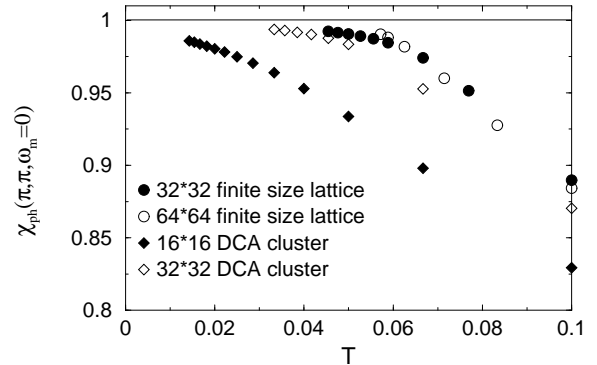


FIG. 10. The FLEX particle-hole bubble ( $\chi_{ph}$ ) at  $Q = (\pi, \pi)$  and  $\omega_m = 0$  for a  $16 \times 16$  and  $32 \times 32$  DCA clusters (diamonds) and also for  $32 \times 32$  and  $64 \times 64$  finite size lattices with periodic boundary conditions (circles) versus temperature  $T$  at  $U/t = 1.57$ . The relatively rapid saturation of the finite size lattice  $\chi_{ph}$  compared to the more gradual approach of the DCA results towards unity is manifest ( $128 \times 128$  finite size lattice results were obtained by Deisz *et al.* [9]).

Earlier in Fig. 10 it was shown that the FLEX particle-hole bubble  $\chi_{ph}(q, \omega_m = 0)$  at  $q = Q = (\pi, \pi)$  approaches unity as the temperature is lowered. This causes the spin-fluctuation  $T$  matrix

$$T_{\sigma, \sigma}(q, \omega_m) = \frac{3}{2} \left[ \frac{\chi_{ph}(q, \omega_m)^2}{1 - \chi_{ph}(q, \omega_m)} \right], \quad (28)$$

which is just the third term in  $V^{(ph)}(q, \omega_m)$  in Eq. 23 to peak around the  $(Q, \omega_m = 0)$  point. For real frequencies,  $T_{\sigma, \sigma}(Q, \omega)$  has a sharp peak around  $\omega = 0$ . Since  $T_{\sigma, \sigma}(Q, \omega)$  is only used to construct the irreducible self-energy, within the DCA it is constructed from coarse-grained Green functions. Thus, the DCA counterpart of Eq. 28 is obtained by only replacing the  $\chi_{ph}$  with  $\chi_{ph}^{DCA}$  defined in Eq. 27. Fig. 13 and Fig. 14 show how this peak sharpens as the temperature decreases or interaction increases for finite size lattices and the DCA respectively. In the  $64 \times 64$  finite size lattice (c.f. Fig 13 bottom), the peak continues to develop as the temperature is lowered and the interaction is raised. At  $T = 0.067$  and  $U = 1.6$  where there exists a pseudogap in the DOS, the peak undergoes a significant growth compared to the other graphs shown in the same figure. The  $32 \times 32$  (c.f. Fig 13.top) lattice presents the same behavior with a slightly sharper but shorter peak.

The DCA also illustrates the same type of peaks at a slightly higher interaction and lower temperatures for the  $16 \times 16$  cluster (c.f. Fig 14 top). Increasing the cluster size to  $32 \times 32$  gives rise to higher peaks similar to the finite size lattices case but unlike the finite size lattices peaks become sharper as the size is increased.

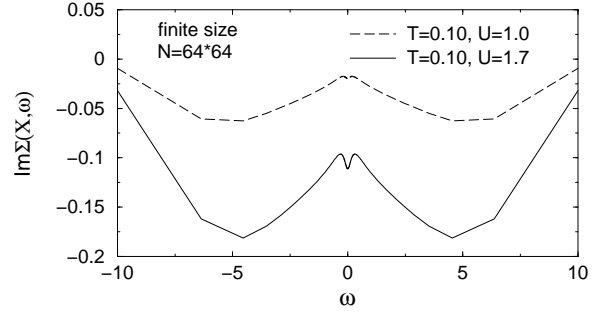
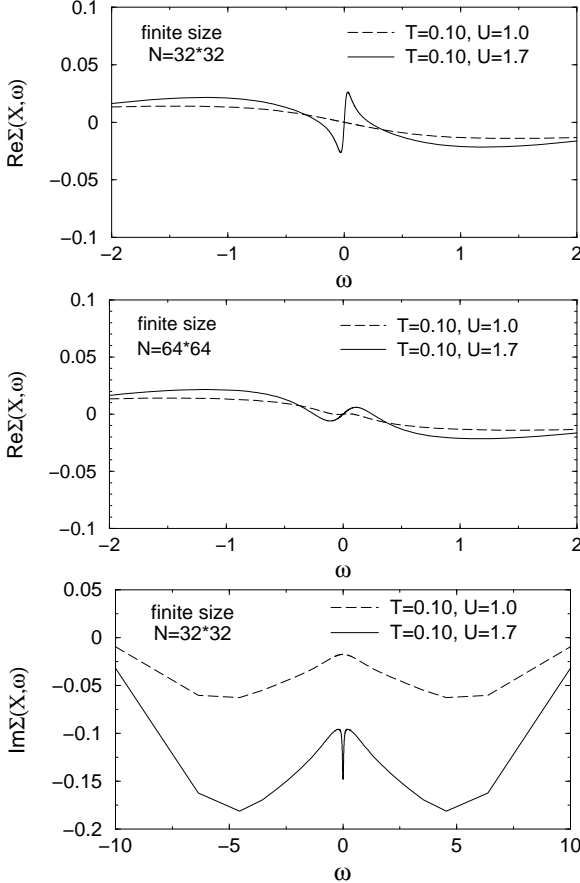
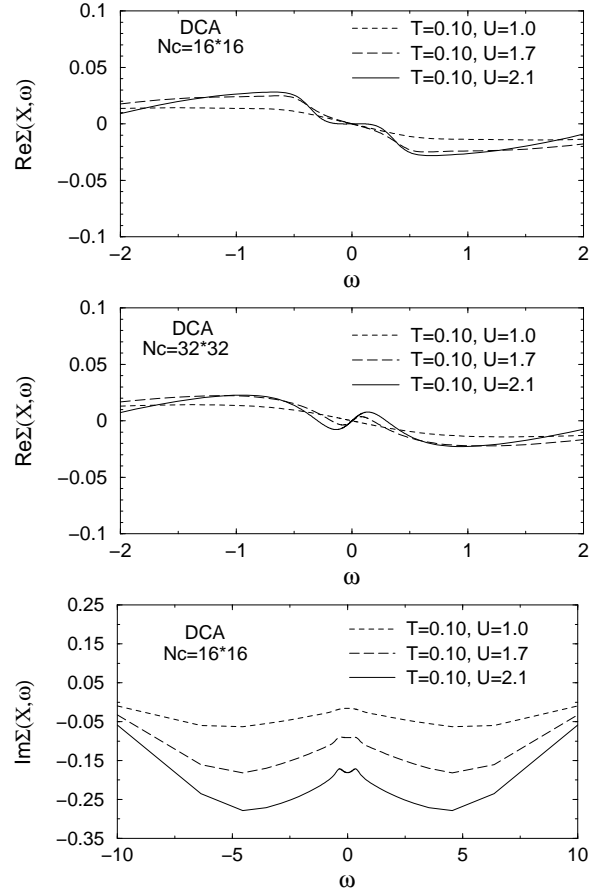


FIG. 11. The FLEX real (top two) and imaginary (bottom two) parts of the self-energy at the X point for  $32 \times 32$  and  $64 \times 64$  finite size lattices with periodic boundary conditions versus energy for  $T = 0.10$  and two different interactions  $U$ . The inverted peak at  $\omega = 0$  in the imaginary part and the positive slope in the real part are both signatures of non-Fermi-liquid behavior. For smaller lattice sizes these signatures are more pronounced ( $128 \times 128$  finite size lattice results were obtained by Deisz *et al.* [9]).



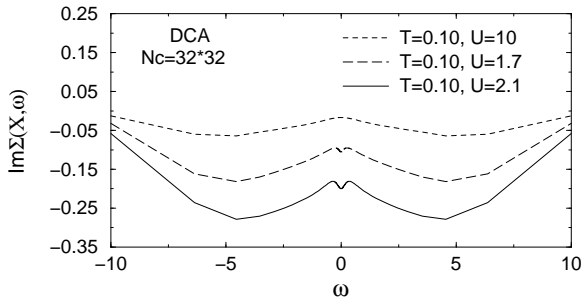


FIG. 12. The FLEX real (top two) and imaginary (bottom two) parts of the self-energy at the X point for  $16 \times 16$  and  $32 \times 32$  DCA clusters versus energy for  $T = 0.10$  and two different interactions  $U$ . The non-Fermi-liquid features occur at slightly higher interactions compared to the finite size lattices. Upon increasing the cluster size, these features become more pronounced (complementary to the finite size lattices with periodic boundary conditions).

All the results illustrated in this section indicate the complementarity of the DCA to the finite size lattice scheme. It is also observed that the DCA is capable of reproducing relatively the same physics as the finite size FLEX at slightly different parameters but a lower CPU cost. The combination of these two facts makes this technique a good candidate to be employed in the numerical treatment of a wide range of many-body problems.

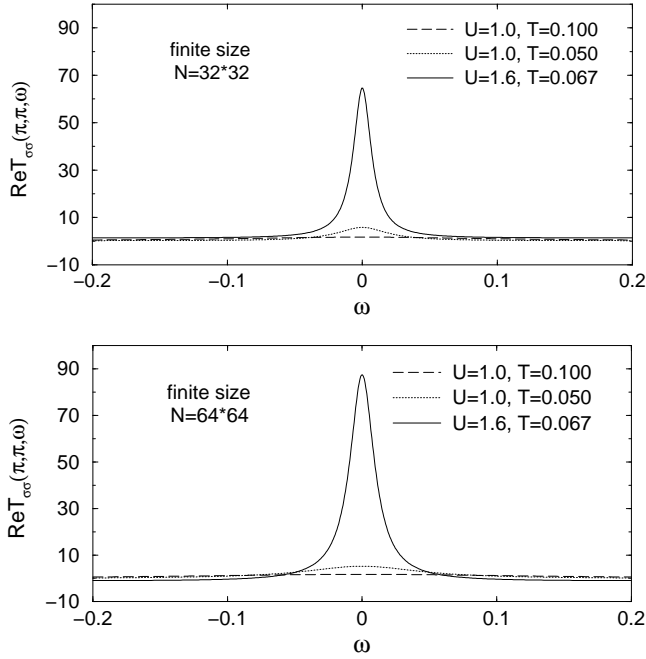


FIG. 13. The FLEX real part of the T-matrix at  $Q = (\pi, \pi)$  versus energy for  $32 \times 32$  (top) and  $64 \times 64$  (bottom) finite size lattices with periodic boundary conditions. For the  $32 \times 32$  finite size lattice at  $T = 0.067$  and  $U/t = 1.6$  (solid), we observe a huge peak due to the formation of a pseudogap in the DOS. By increasing the lattice size to  $64 \times 64$  a higher and broader peak occurs at the same temperature.

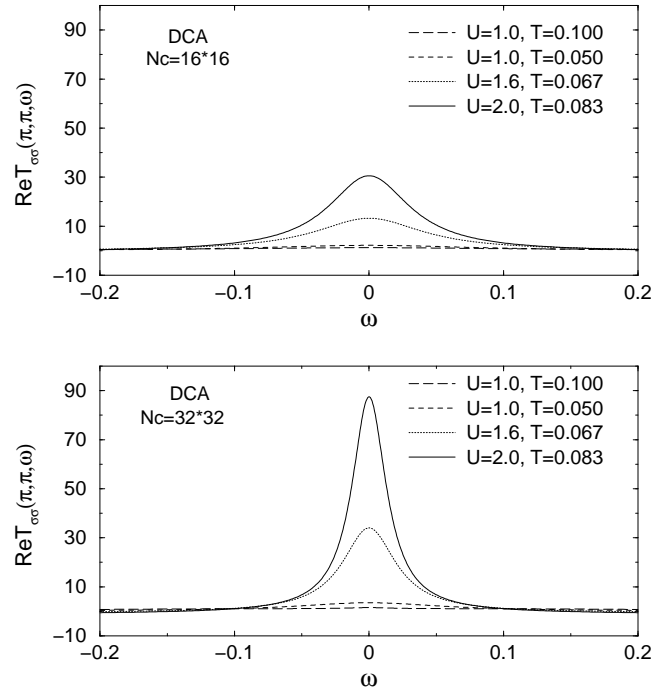


FIG. 14. The FLEX real part of the T-matrix at  $Q = (\pi, \pi)$  versus energy for  $16 \times 16$  (top) and  $32 \times 32$  (bottom) DCA clusters. Peaks similar to the finite size lattices appear at slightly higher interactions and lower temperatures. By increasing the cluster size, the peaks grow higher (similar to finite size lattices) and also sharpen (complementary to the finite size lattices).

Lastly, to better understand the effect of the DCA cluster embedded in a Fermionic bath, we can rewrite the coarse grained Green function defined in Eq. 5 as

$$\bar{G}(\mathbf{K}, z) = \frac{1}{z - \bar{\epsilon}_{\mathbf{K}} - \Sigma(\mathbf{K}, z) - \Gamma(\mathbf{K}, z)}. \quad (29)$$

where  $\bar{\epsilon}_{\mathbf{K}} = N_c/N \sum_{\tilde{\mathbf{k}}} \epsilon_{\mathbf{K}+\tilde{\mathbf{k}}}$  and  $\Gamma(\mathbf{K}, z)$  is the host function. Maier *et al.* [6], define

$$t_{\mathbf{K}+\tilde{\mathbf{k}}} = \epsilon_{\mathbf{K}+\tilde{\mathbf{k}}} - \bar{\epsilon}_{\mathbf{K}}, \quad (30)$$

whereby  $\Gamma(\mathbf{K}, z)$  can be expressed as

$$\Gamma(\mathbf{K}, z) = \frac{\frac{N_c}{N} \sum_{\tilde{\mathbf{k}}} t_{\mathbf{K}+\tilde{\mathbf{k}}}^2 G(\mathbf{K} + \tilde{\mathbf{k}}, z)}{1 + \frac{N_c}{N} \sum_{\tilde{\mathbf{k}}} t_{\mathbf{K}+\tilde{\mathbf{k}}} G(\mathbf{K} + \tilde{\mathbf{k}}, z)}. \quad (31)$$

By Taylor expanding  $t_{\mathbf{K}+\tilde{\mathbf{k}}}$  around the cluster points  $\mathbf{K}$  it is found that  $t_{\mathbf{K}+\tilde{\mathbf{k}}} \sim \mathcal{O}(\Delta k)$  with  $\Delta k = 2\pi/L$ . Thus, Eq. 31 yields  $\Gamma(\mathbf{K}) \sim \mathcal{O}((\Delta k)^2)$  as  $\Delta k \rightarrow 0$ . To illustrate this, we calculate  $\Gamma(r = 0, \tau = 0)$  by summing over all the  $\mathbf{K}$  points and  $\omega_n$  frequencies and plot it versus  $(\Delta k)^2$ . Fig. 15 illustrates this linear behavior for  $N_c \geq 16$ .  $N_c = 1$  holds complete mean field characters and no non-local fluctuations.  $N_c = 4$  is anomalous as explained in an article by Betts *et al.* [15]. There, the finite size cubic lattices with less than six (four in 2D

square lattices) distinct nearest neighbors per each site are not used in finite size scalings for estimating the physical properties of models like the spin one half XY ferromagnet or the Heisenberg antiferromagnet. For  $N_c = 4$ , because of the periodicity of the clusters, each cluster point is surrounded by two identical nearest neighbors in every direction and therefore has only two distinct nearest neighbors (c.f. Fig. 16). Thus, the effect of fluctuations are overestimated. [21] For  $N_c > 4$  there is no such anomaly and hence, all the points present the linear behavior proven above. Nevertheless, calculations with  $N_c = 4$  do a reasonable job in capturing the qualitative effects of corrections to the DMFA.

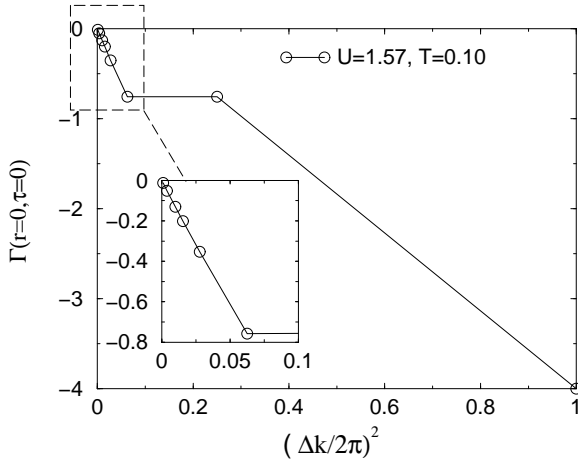


FIG. 15. The host function  $\Gamma(r = 0, \tau = 0)$  versus  $(\Delta k)^2$ . The linear behavior beyond  $N_c = 4$  is manifest, see also the inset.

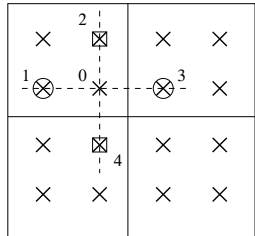


FIG. 16. DCA clusters in the real space lattice with  $N_c = 4$ . Due to the periodicity of the clusters, points 2 and 4 in squares and 1 and 3 in circles are equivalent and therefore point 0 observes its nearest neighbors twice in each direction.

### VIII. MICROSCOPIC THEORY OF THE DCA

In section IV we defined the thermodynamic potential functional difference  $\Delta\Omega(T, \mu)$  in terms of the Green function, self-energy, and  $\Phi[G]$  (c.f. Eq. 25). In Eq. 13,  $\Phi[G]$  includes all the compact (skeletal) Feynman diagrams and the rest incorporates the entire non-compact contribution. [22] Typical compact and non-compact diagrams are illustrated in Fig. 17. The non-compact diagram (a) consists of two self-energy pieces  $\sigma$  and  $\sigma'$  connected with two one-particle Green functions. Removing these two Green functions would split the diagram into two separate pieces. In the compact diagram (b) two vertex parts  $\Gamma$  and  $\Gamma'$  with four Green functions are connected together. One can not split this type of diagrams into two separate pieces by just removing two one-particle Green functions. As mentioned earlier, in the DCA, we employ coarse-grained Green functions to construct only the compact diagrams. The Green functions in non-compact diagrams are calculated directly using Eq. 26 in which the self-energy  $\Sigma_{DCA}(\mathbf{K}, z)$  is coarse-grained (the circles at the top and the bottom of the non-compact diagram in Fig. 17. (a))

connected with two one-particle Green functions. Removing these two Green functions would split the diagram into two separate pieces. In the compact diagram (b) two vertex parts  $\Gamma$  and  $\Gamma'$  with four Green functions are connected together. One can not split this type of diagrams into two separate pieces by just removing two one-particle Green functions. As mentioned earlier, in the DCA, we employ coarse-grained Green functions to construct only the compact diagrams. The Green functions in non-compact diagrams are calculated directly using Eq. 26 in which the self-energy  $\Sigma_{DCA}(\mathbf{K}, z)$  is coarse-grained (the circles at the top and the bottom of the non-compact diagram in Fig. 17. (a))

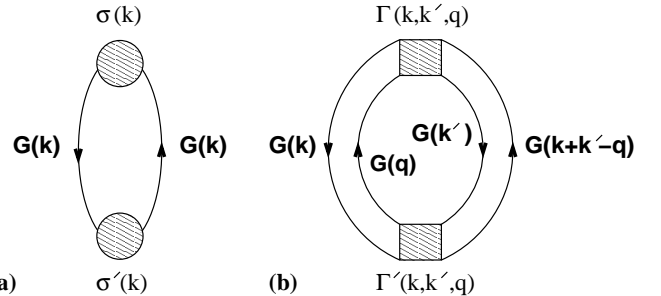


FIG. 17. (a) typical non-compact (non-skeletal) and (b) typical compact (skeletal) diagrams.

Earlier in a shorter article for the Hubbard model in particular [11], we showed both analytically and numerically that the error produced by coarse-graining the non-compact diagrams is significantly larger than the error produced by coarse-graining the compact ones. Here, we would like to give a more general argument in real space. We wish to emphasize two points in this new approach. First, since the derivation of the DCA in this section relies only upon the exponential fall off of the Green function as a function of distance, it is far more intuitive than the momentum space argument in Ref. [11]. Second, it ties the derivation of the DCA to the original derivation of the DMFA in the limit of infinite dimensions, where similar arguments are employed. [14]

The exponential fall off behavior occurs naturally in high dimensions. In the tight-binding Hamiltonian (c.f. Eq. 8), the factor  $t$  corresponds to the hopping of electrons among nearest neighboring sites. Thus, one could show that the real space Green function  $G(r)$  (we drop the frequency label from this point on for simplicity) for  $r$  nearest neighbor hops is proportional to  $G(r) \sim t^r$  as  $t \rightarrow 0$ . On the other hand, Metzner *et al.*, and Müller-Hartmann [14,13] have shown that in  $D$  dimensions, the factor  $t$  should be renormalized as  $t/\sqrt{D}$  in order to have a finite density of states width as  $D \rightarrow \infty$ . As a result of this renormalization

$$G(r) \sim t^r \sim (1/\sqrt{D})^r \sim D^{-r/2} = e^{-r/r_s}$$

$$r_s = \frac{2}{\ln D}, \quad (32)$$

meaning that  $G(r)$  falls off exponentially as a function of

r.

In the DCA, we attempt to minimize the error due to coarse-graining the Green function (and potentials) in the Feynman diagrams. Consider the first non-trivial correction to the coarse-grained non-compact diagrams generated by replacing the explicit coarse-grained Green function lines by the non-coarse-grained ones as illustrated in Fig. 18

$$\delta^{(1)}[\Delta\Omega_{ncp}] \sim \frac{1}{N} \sum_{\mathbf{k}} \sigma(\mathbf{K}) \sigma'(\mathbf{K}) G(\mathbf{k})^2 - \frac{1}{N_c} \sum_{\mathbf{K}} \sigma(\mathbf{K}) \sigma'(\mathbf{K}) \bar{G}(\mathbf{K})^2, \quad (33)$$

where  $\mathbf{K}$  are the coarse-graining cells momenta and  $\mathbf{k} = \mathbf{K} + \tilde{\mathbf{k}}$  include all the momenta in the first Brillouin zone shown in Fig. 2. In this derivation we also presume that the self-energy is  $\tilde{\mathbf{k}}$  independent and the entire  $\tilde{\mathbf{k}}$  dependence is embedded in the Green functions.

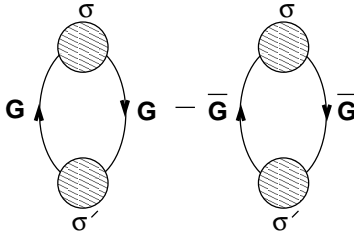


FIG. 18. First correction by non-compact diagrams,  $\delta^{(1)}[\Delta\Omega_{ncp}]$ .

By breaking up the sums over  $\mathbf{k}$  in Eq. 33 into  $\mathbf{K}$  and  $\tilde{\mathbf{k}}$  sums and writing all the  $G$  in terms of their Fourier transforms at the same time we get

$$\delta^{(1)}[\Delta\Omega_{ncp}] \sim \frac{1}{N} \sum_{\mathbf{k}, \mathbf{K}} \sigma(\mathbf{K}) \sigma'(\mathbf{K}) \sum_{\mathbf{x}_1, \mathbf{x}_2} G(\mathbf{x}_1) G(\mathbf{x}_2) \times e^{-i\tilde{\mathbf{k}} \cdot (\mathbf{x}_1 + \mathbf{x}_2)} e^{-i\mathbf{K} \cdot (\mathbf{x}_1 + \mathbf{x}_2)} - \frac{N_c}{N^2} \sum_{\mathbf{K}, \tilde{\mathbf{k}}_1, \tilde{\mathbf{k}}_2} \sigma(\mathbf{K}) \sigma'(\mathbf{K}) \times \sum_{\mathbf{x}_1, \mathbf{x}_2} G(\mathbf{x}_1) G(\mathbf{x}_2) e^{-i\tilde{\mathbf{k}}_1 \cdot \mathbf{x}_1} e^{-i\tilde{\mathbf{k}}_2 \cdot \mathbf{x}_2} e^{-i\mathbf{K} \cdot (\mathbf{x}_1 + \mathbf{x}_2)}, \quad (34)$$

in which we used Eq. 5 for  $\bar{G}(\mathbf{K})$ . According to Fig. 2, we can split  $\mathbf{x} = \mathbf{X} + \tilde{\mathbf{x}}$  where  $\tilde{\mathbf{x}}$  extend between two separate clusters while  $\mathbf{X}$  always remain within a single cluster. By making this separation in Eq. 34 one picks up phases including products of  $-i\mathbf{K} \cdot \mathbf{X}$ ,  $-i\mathbf{K} \cdot \tilde{\mathbf{x}}$ ,  $-i\tilde{\mathbf{k}} \cdot \mathbf{X}$  and  $-i\tilde{\mathbf{k}} \cdot \tilde{\mathbf{x}}$  in their exponents. The phase associated with the product  $\mathbf{K} \cdot \tilde{\mathbf{x}} = 2n\pi$  with  $n$  an integer equals unity. The phases involving  $-i\tilde{\mathbf{k}} \cdot \mathbf{X}$  products are also neglected as discussed in section II. Hence, Eq. 34 can be rewritten as follows

$$\delta^{(1)}[\Delta\Omega_{ncp}] \sim \frac{1}{N} \sum_{\mathbf{K}} \sigma(\mathbf{K}) \sigma'(\mathbf{K}) \sum_{\mathbf{X}_1, \mathbf{X}_2} \sum_{\tilde{\mathbf{x}}_1, \tilde{\mathbf{x}}_2} G(\mathbf{X}_1 + \tilde{\mathbf{x}}_1) \times G(\mathbf{X}_2 + \tilde{\mathbf{x}}_2) e^{-i\mathbf{K} \cdot (\mathbf{X}_1 + \mathbf{X}_2)} \sum_{\tilde{\mathbf{k}}} e^{-i\tilde{\mathbf{k}} \cdot (\tilde{\mathbf{x}}_1 + \tilde{\mathbf{x}}_2)} - \frac{N_c}{N^2} \sum_{\mathbf{K}} \sigma(\mathbf{K}) \times$$

$$\sigma'(\mathbf{K}) \sum_{\mathbf{X}_1, \mathbf{X}_2} \sum_{\tilde{\mathbf{x}}_1, \tilde{\mathbf{x}}_2} G(\mathbf{X}_1 + \tilde{\mathbf{x}}_1) \mathbf{G}(\mathbf{X}_2 + \tilde{\mathbf{x}}_2) e^{-i\mathbf{K} \cdot (\mathbf{X}_1 + \mathbf{X}_2)} \times \sum_{\tilde{\mathbf{k}}_1, \tilde{\mathbf{k}}_2} e^{-i\tilde{\mathbf{k}}_1 \cdot \mathbf{x}_1} e^{-i\tilde{\mathbf{k}}_2 \cdot \mathbf{x}_2}. \quad (35)$$

Implementing the following substitutions

$$\sum_{\tilde{\mathbf{k}}} e^{-i\tilde{\mathbf{k}} \cdot (\tilde{\mathbf{x}}_1 + \tilde{\mathbf{x}}_2)} = \frac{N}{N_c} \delta_{\tilde{\mathbf{x}}_1, -\tilde{\mathbf{x}}_2} \quad \text{and} \quad \sum_{\tilde{\mathbf{k}}_1, \tilde{\mathbf{k}}_2} e^{-i\tilde{\mathbf{k}}_1 \cdot \mathbf{x}_1} e^{-i\tilde{\mathbf{k}}_2 \cdot \mathbf{x}_2} = \left(\frac{N}{N_c}\right)^2 \delta_{\tilde{\mathbf{x}}_1, 0} \delta_{\tilde{\mathbf{x}}_2, 0}, \quad (36)$$

Eq. 35 simplifies into

$$\delta^{(1)}[\Delta\Omega_{ncp}] \sim \frac{1}{N_c} \sum_{\mathbf{K}} \sigma(\mathbf{K}) \sigma'(\mathbf{K}) \left[ \sum_{\mathbf{X}_1, \mathbf{X}_2, \tilde{\mathbf{x}}} G(\mathbf{X}_1 + \tilde{\mathbf{x}}) \times \mathbf{G}(\mathbf{X}_2 - \tilde{\mathbf{x}}) e^{-i\mathbf{K} \cdot (\mathbf{X}_1 + \mathbf{X}_2)} - \sum_{\mathbf{X}_1, \mathbf{X}_2} G(\mathbf{X}_1) \mathbf{G}(\mathbf{X}_2) \times e^{-i\mathbf{K} \cdot (\mathbf{X}_1 + \mathbf{X}_2)} \right]. \quad (37)$$

Setting  $\sigma(\mathbf{K}) \sigma'(\mathbf{K}) = \xi(\mathbf{K})$  and performing the  $\mathbf{K}$  summation

$$\delta^{(1)}[\Delta\Omega_{ncp}] \sim \sum_{\mathbf{X}_1, \mathbf{X}_2} \xi(\mathbf{X}_1 + \mathbf{X}_2) \left[ \sum_{\tilde{\mathbf{x}}} G(\mathbf{X}_1 + \tilde{\mathbf{x}}) \times \mathbf{G}(\mathbf{X}_2 - \tilde{\mathbf{x}}) - G(\mathbf{X}_1) \mathbf{G}(\mathbf{X}_2) \right] = \sum_{\mathbf{X}_1, \mathbf{X}_2} \xi(\mathbf{X}_1 + \mathbf{X}_2) \times \sum_{\tilde{\mathbf{x}} \neq 0} G(\mathbf{X}_1 + \tilde{\mathbf{x}}) \mathbf{G}(\mathbf{X}_2 - \tilde{\mathbf{x}}). \quad (38)$$

Knowing that  $\xi(\mathbf{X}_1 + \mathbf{X}_2) = \sum_{\mathbf{X}} \sigma(\mathbf{X}) \sigma'(\mathbf{X} + \mathbf{X}_1 + \mathbf{X}_2)$  and also that the lowest order of  $\sigma(\mathbf{X}) \sim G^3(\mathbf{X}) \sim e^{-3|\mathbf{X}|/r_s}$  we conclude that in Eq. 38, the largest contribution is due to terms having  $\mathbf{X}_1 = -\mathbf{X}_2$  or in other words, local  $\xi$ . As shown in Fig. 19, the first term in the  $\tilde{\mathbf{x}}$  sum corresponds to  $|\tilde{\mathbf{x}}| = L$  (size of the cluster) and  $\mathbf{X}$  can be as large as  $\mathbf{X} = -(L-1)$  in the opposite direction. Hence, the leading order term in Eq. 38 falls off as

$$\delta^{(1)}[\Delta\Omega_{ncp}] \sim \xi(0) \times 2D \times G(L - (L-1)) \times G(-L + (L-1)) \sim 2D\xi(0) e^{\frac{-1}{r_s}} e^{\frac{-1}{r_s}} = 2D\xi(0) e^{\frac{-2}{r_s}}, \quad (39)$$

where  $2D$  is the number of  $|\tilde{\mathbf{x}}| = L$  contributions in  $D$  different dimensions of a  $D$  dimensional cubic lattice. In Eq. 39 we also used the fact that due to the lattice symmetry,  $G(-\mathbf{X}) = G(\mathbf{X})$ . As  $D \rightarrow \infty$ , using  $r_s = 2/\ln D$

$$\delta^{(1)}[\Delta\Omega_{ncp}] \sim 2D\xi(0) e^{-\ln D} = 2\xi(0) D D^{-1} \sim \mathcal{O}(1). \quad (40)$$

which indicates the existence of non-local corrections to the non-compact contribution of the thermodynamic potential even at infinite dimensions.

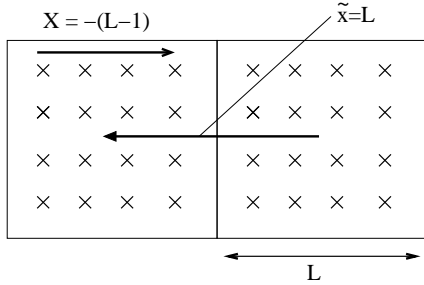


FIG. 19. Two adjacent clusters with their  $\mathbf{X}$  and  $\tilde{\mathbf{x}}$  vectors.

Now we replace the coarse-grained self-energy bubbles in Fig. 18 with coarse-grained vertices having four external legs and look at the difference between compact diagrams with and without coarse-grained Green functions which are explicitly shown in the figure. Since we earlier dropped the frequency labels in the Green functions, here we use indices 1, 2, 3 and 4 to emphasize that these Green functions have different frequency labels. The first correction to the compact contribution of the thermodynamic potential depicted in Fig. 20 is

$$\begin{aligned} \delta^{(1)}[\Delta\Omega_{cp}] \sim & \frac{1}{N^3} \sum_{\mathbf{k}_1, \mathbf{k}_2} \Gamma(\mathbf{K}_1, \mathbf{K}_2, \mathbf{Q}) \Gamma'(\mathbf{K}_1, \mathbf{K}_2, \mathbf{Q}) G_1(\mathbf{k}_1) \times \\ & G_2(\mathbf{k}_2) G_3(\mathbf{q}) G_4(\mathbf{k}_1 + \mathbf{k}_2 - \mathbf{q}) - \frac{1}{N_c^3} \sum_{\mathbf{k}_1, \mathbf{k}_2} \Gamma(\mathbf{K}_1, \mathbf{K}_2, \mathbf{Q}) \times \\ & \Gamma'(\mathbf{K}_1, \mathbf{K}_2, \mathbf{Q}) \bar{G}_1(\mathbf{K}_1) \bar{G}_2(\mathbf{K}_2) \bar{G}_3(\mathbf{Q}) \bar{G}_4(\mathbf{K}_1 + \mathbf{K}_2 - \mathbf{Q}), \end{aligned} \quad (41)$$

where similar to Eq. 33, all the vertices are coarse-grained but the Green functions are not.

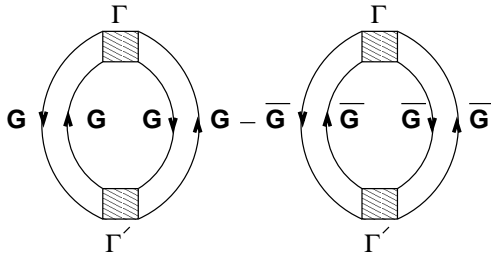


FIG. 20. First correction by compact diagrams,  $\delta^{(1)}[\Delta\Omega_{cp}]$ .

Following the same procedure as for the non-compact difference we arrive at

$$\begin{aligned} \delta^{(1)}[\Delta\Omega_{cp}] \sim & \sum_{\mathbf{x}_1, \mathbf{x}_2} \Lambda(\mathbf{X}_1 + \mathbf{X}_4, \mathbf{X}_2 + \mathbf{X}_4, \mathbf{X}_3 - \mathbf{X}_4) \times \\ & \left[ \sum_{\tilde{\mathbf{x}}} G_1(\mathbf{X}_1 - \tilde{\mathbf{x}}) G_2(\mathbf{X}_2 - \tilde{\mathbf{x}}) G_3(\mathbf{X}_3 + \tilde{\mathbf{x}}) G_4(\mathbf{X}_4 + \tilde{\mathbf{x}}) - \right. \\ & \left. G_1(\mathbf{X}_1) G_2(\mathbf{X}_2) G_3(\mathbf{X}_3) G_4(\mathbf{X}_4) \right], \end{aligned} \quad (42)$$

where

$$\begin{aligned} \Lambda(\mathbf{X}_1 + \mathbf{X}_4, \mathbf{X}_2 + \mathbf{X}_4, \mathbf{X}_3 - \mathbf{X}_4) = & \frac{1}{N_c^3} \sum_{\substack{\mathbf{K}_1, \mathbf{K}_2 \\ \mathbf{Q}}} \Gamma(\mathbf{K}_1, \mathbf{K}_2, \mathbf{Q}) \times \\ \Gamma'(\mathbf{K}_1, \mathbf{K}_2, \mathbf{Q}) e^{-i\mathbf{K}_1 \cdot (\mathbf{X}_1 + \mathbf{X}_4)} e^{-i\mathbf{K}_2 \cdot (\mathbf{X}_2 + \mathbf{X}_4)} e^{-i\mathbf{Q} \cdot (\mathbf{X}_3 - \mathbf{X}_4)} = \\ \sum_{\substack{\mathbf{x}, \mathbf{x}' \\ \mathbf{x}''}} \Gamma(\mathbf{X}, \mathbf{x}', \mathbf{x}'') \times \\ \Gamma'(\mathbf{X} + \mathbf{X}_1 + \mathbf{X}_4, \mathbf{x}' + \mathbf{X}_2 + \mathbf{X}_4, \mathbf{x}'' + \mathbf{X}_3 - \mathbf{X}_4). \end{aligned} \quad (43)$$

Once again, the largest contribution is associated with local  $\Lambda$ , i.e.,  $\mathbf{X}_1 = -\mathbf{X}_4$ ,  $\mathbf{X}_2 = -\mathbf{X}_4$  and  $\mathbf{X}_3 = \mathbf{X}_4$ . Therefore

$$\begin{aligned} \delta^{(1)}[\Delta\Omega_{cp}] \sim & \sum_{\mathbf{X}} \Lambda(0) \left[ \sum_{\tilde{\mathbf{x}}} G_1(-\mathbf{X} - \tilde{\mathbf{x}}) G_2(-\mathbf{X} - \tilde{\mathbf{x}}) \times \right. \\ & G_3(\mathbf{X} + \tilde{\mathbf{x}}) G_4(\mathbf{X} + \tilde{\mathbf{x}}) - G_1(\mathbf{X}) G_2(\mathbf{X}) G_3(\mathbf{X}) G_4(\mathbf{X}) \left. \right] = \\ & \Lambda(0) \sum_{\mathbf{X}, \tilde{\mathbf{x}} \neq 0} G_1(\mathbf{X} + \tilde{\mathbf{x}}) G_2(\mathbf{X} + \tilde{\mathbf{x}}) G_3(\mathbf{X} + \tilde{\mathbf{x}}) G_4(\mathbf{X} + \tilde{\mathbf{x}}). \end{aligned} \quad (44)$$

Considering  $|\tilde{\mathbf{x}}| = L$  and  $\mathbf{X}_{min} = -(L-1)$

$$\begin{aligned} \delta^{(1)}[\Delta\Omega_{cp}] \sim & \Lambda(0) \times 2D \times G_1(-L + (L-1)) \times \\ & G_2(-L + (L-1)) G_3(L - (L-1)) G_4(L - (L-1)) = \\ & 2D \Lambda(0) e^{\frac{-4}{rs}} = 2\Lambda(0) D^{-1}, \quad (r_s = \frac{2}{\ln D}) \end{aligned} \quad (45)$$

which vanishes as  $D \rightarrow \infty$ .

Comparing Eq. 45 with Eq. 40 shows that the first correction to the compact contribution of the thermodynamic potential falls off exponentially twice as fast as the equivalent correction in the non-compact contribution. In addition, even at the infinite dimensional limit, there are corrections of order one to the non-compact contribution whereas for the compact diagrams the DCA becomes exact and there are no corrections. This justifies coarse-graining only in the compact diagrams. The Green functions in the non-compact diagrams have to be explicitly constructed from the coarse-grained self-energy  $\Sigma_{DCA}(\mathbf{K}, \omega_n)$  using Eq. 26.

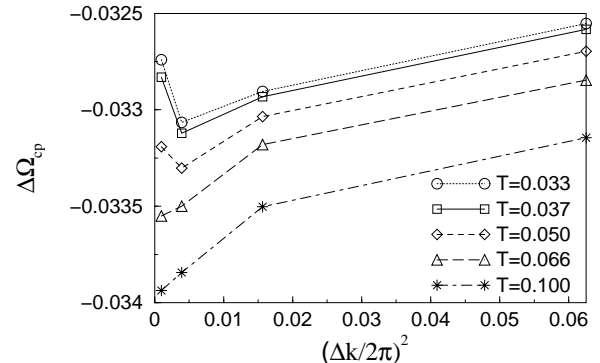


FIG. 21. The compact contribution to the thermodynamic potential versus  $(\Delta k)^2$  at  $U/t = 1.57$  and various temperatures, using coarse-grained Green functions. The deviation from linearity at the lowest temperatures hint at the correlation length exceeding the cluster size.

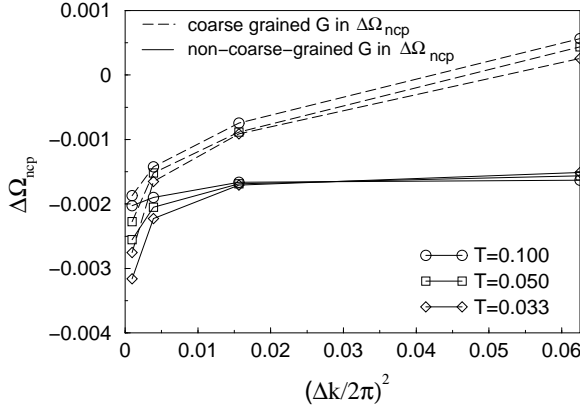


FIG. 22. Non-compact contribution to the thermodynamic potential versus  $(\Delta k)^2$  at  $U/t = 1.57$  with and without coarse-grained Green functions. Using coarse-grained Green functions can result in a non-compact contribution with the wrong sign.

In Fig. 21, the compact contribution of the thermodynamic potential difference constructed by coarse-grained Green functions is plotted versus  $(\Delta k)^2 = 1/L^2$ . The variation of  $\Delta\Omega_{cp}$  over the entire  $1/L^2$  range is about 1%. At very low temperatures ( $T < 0.066$  in the inset), some deviation from linearity is observed due to the correlation length exceeding the cluster size  $L$  and therefore the approximation of  $\Sigma(k)$  by  $\Sigma_{DCA}(K)$  begins to break down. Fig. 22 illustrates the non-compact contribution sketched versus  $1/L^2$  using both coarse-grained and non-coarse-grained Green functions. Using non-coarse-grained Green functions, the variation of  $\Delta\Omega_{ncp}$  over the entire  $1/L^2$  range is roughly 30%. Coarse-graining the Green functions in these diagrams can even change the sign of this non-compact contributions, clearly indicating that coarse-graining the Green function is an unrealistic approximation for non-compact diagrams. However, one notices that for large cluster sizes the coarse-grained and non-coarse-grained results approach each other as the approximation to the infinite lattice becomes better.

## IX. DCA IN FREQUENCY SPACE

As illustrated for the momentum space, the DCA results in a significant reduction of the problem complexity and it is complementary to the finite size lattice approach. In analogy to the momentum space, one could consider dividing the one dimensional Matsubara frequency space into a number of coarse-graining subcells. For both fermions and bosons, each cell should include an odd number of frequencies in order for the frequencies in the centers of these cells to preserve Fermionic or Bosonic properties. Fig. 23 represents how the frequency space can be divided into coarse-graining subcells each comprising a central  $\Omega_n$  frequency and a number of coarse-graining  $\tilde{\omega}_n$  lying around it. The central  $\Omega_n$  frequencies can be rewritten in the form of the original lattice with

renormalized  $\beta$  shown as  $\beta_c$  in the figure. Similar to the case of the momentum space, we make the following transformation for the Laue function

$$\Delta = \beta \delta_{\omega_{n1}, \omega_{n2} + \omega_{n3}} \rightarrow \Delta_{DCA} = \beta_c \delta_{\Omega_{n1}, \Omega_{n2} + \Omega_{n3}}, \quad (46)$$

for the Matsubara frequencies of the vertex shown in Fig. 1 considering frequency dependent interactions in general (in condensed matter physics, most of the interactions are indeed simultaneous and thus frequency independent). As a result, we may again coarse-grain the Green function over the subcell frequencies

$$\bar{G}(\mathbf{K}, \Omega_n) = \frac{\beta_c}{\beta} \sum_{\tilde{\omega}_n} G(\mathbf{K}, \Omega_n + \tilde{\omega}_n). \quad (47)$$

According to Fig. 23, the full coarse-graining of the Green function amounts to  $\beta_c \rightarrow 0$  which causes all the self-energy Feynman diagrams ordered higher than first (Hartree-Fock diagrams) to vanish and consequently we arrive at a fully static problem.

Unfortunately, we can show that coarse-graining over Matsubara frequencies can lead to the violation of causality and as a result, the DCA is not systematically implementable for the Matsubara frequency quantities. The simplest example is the non-interacting Green function coarse-grained as follows [23]

$$\begin{aligned} \bar{G}^{(0)}(\mathbf{K}, \Omega_n) &= \frac{\beta_c}{\beta} \sum_{\tilde{\omega}_n} G^{(0)}(\mathbf{K}, \Omega_n + \tilde{\omega}_n) = \\ &= \frac{\beta_c}{\beta} \sum_{\tilde{\omega}_n} \frac{1}{i\Omega_n + i\tilde{\omega}_n - \epsilon_k + \mu}. \end{aligned} \quad (48)$$

The retarded Green function is derived by the substitution  $i\Omega_n \rightarrow \Omega + i\eta$

$$\bar{G}_{ret}^{(0)}(\mathbf{K}, \Omega) = \frac{\beta_c}{\beta} \sum_{\tilde{\omega}_n} \frac{1}{\Omega + i\eta + i\tilde{\omega}_n - \epsilon_k + \mu}. \quad (49)$$

The theory of analytic functions of a complex variable tells us that in order for the Green function to remain retarded in the time space,  $\bar{G}_{ret}^{(0)}(\mathbf{K}, \Omega)$  must not have any poles in the upper half plane of  $\Omega$ . In Eq. 49, one could readily create poles in the upper half plane for negative  $\tilde{\omega}_n$  which causes causality violation and consequently unphysical results.

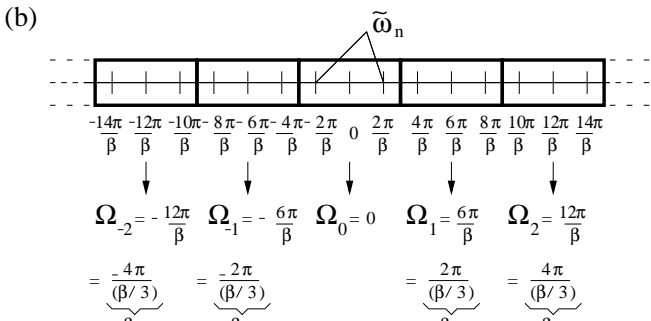
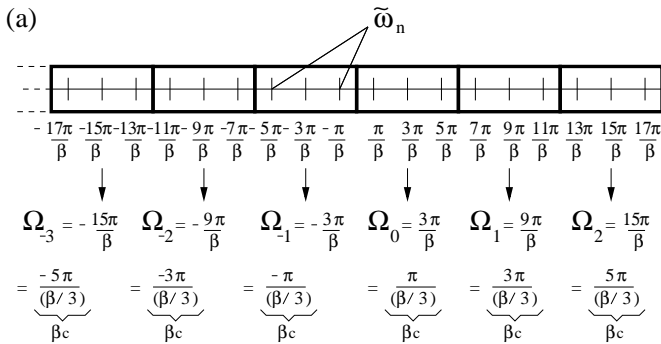


FIG. 23. Dividing the fermion (a) and boson (b) Matsubara frequency spaces into subcells. The central  $\Omega_n$  frequencies can be written in the form of the original lattice with renormalized  $\beta$  denoted as  $\beta_c$  ( $\beta_c = \beta/3$  in this case).

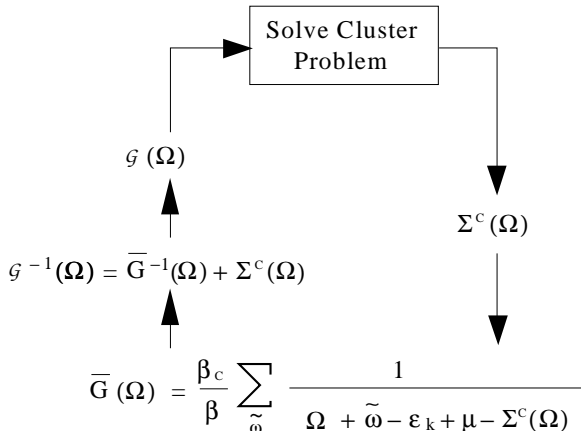


FIG. 24. The algorithm for the cluster solvers such as the NCA in which at each step before using the cluster solver the bare Green function is calculated by excluding the cluster self-energy. This is the only step through the algorithm where problems with causality might occur.

The way around this difficulty is to use real frequencies even at finite temperatures. By invoking real frequencies we no longer coarse-grain over imaginary values. Therefore, the retarded Green function will never acquire poles in the upper half plane and remains causal as shown below

$$\bar{G}_{ret}(\mathbf{K}, \Omega) =$$

$$\frac{N_{\tilde{\omega}}}{N_{\omega}} \sum_{\tilde{\omega}} \frac{1}{\Omega + \tilde{\omega} + i\eta + -\epsilon_k + \mu - \Sigma_{ret}(\mathbf{K}, \Omega)}, \quad (50)$$

with  $N_{\omega}$  the total number of frequencies and  $N_{\tilde{\omega}}$  the number of those we coarse-graining over in each cell. In an article by Hettler *et al.* [4], a formal proof of causality is given (based on a geometrical argument) for coarse-graining in the momentum space. This proof can be straightforwardly applied to the real frequency space as well and it extends the application of real frequency DCA not only to the perturbative cluster solvers such as the FLEX but also techniques like the NCA.

Lastly, similar to the momentum space, care must be taken when choosing the the size of the frequency coarse-graining cells. One must make sure that the cells are not larger than some characteristic energy scale (e.g. the Kondo temperature  $T_K$ ) as the coarse-graining would then suppress the relevant physics.

## X. CONCLUSIONS AND OUTLOOK

We introduce and examine the DCA in detail by employing it with the FLEX to study the half filled two dimensional Hubbard model. The FLEX is not as precise as nearly exact techniques such as quantum Monte Carlo in describing the Hubbard model at strong interaction regime. However, it is capable of illustrating the utility of the DCA, including the complementarity and convergence of the DCA compared to finite size lattice approaches. The DCA and finite size calculations (with periodic boundary conditions) both converge with corrections  $\mathcal{O}(\lambda/L^2)$ ; however, in our example the coefficient  $\lambda_{DCA}$  was smaller and of opposite sign than  $\lambda_{FS}$ , indicating that the DCA converges more quickly and from a complementary direction. This complementarity was also seen in other quantities such as the pseudogap in the density of state and the non-Fermi liquid behaviour that the DCA (finite size) calculation systematically under (over) estimates.

We also provide a detailed microscopic definition of the DCA by inspecting the the error generated by coarse-graining the Green functions in the compact and non-compact contributions to the thermodynamic potential. We conclude that due to the large magnitude of error that it generates, coarse-graining the Green function in non-compact part should be avoided and only the compact contribution should undergo coarse-graining. It also appears that coarse-graining the Green functions over the Matsubara frequencies can and will lead to the violation of causality and therefore is pathological. Nevertheless, one can coarse-grain the Green function over real frequencies and preserve the causality not only for the FLEX but also cluster solvers such as NCA in which the cluster contribution to the coarse-grained dressed Green function is excluded before being inserted in the cluster solver.

The outlook for the FLEX-DCA approach is promising. Although the FLEX fails to accurately describe short-

ranged physics such as moment formation (and related phenomena like the Mott gap), it does a good job describing long-ranged physics associated with spin and charge fluctuations. On the other hand, numerically exact calculations such as QMC, are too expensive to perform for large clusters, and are thus restricted to the study of short-length scales. However, since the DCA gives us a way of parsing the problem into different length scales, it may be used to combine the short-length scale information from the QMC with the long length scale information from the FLEX. This may be accomplished, by embedding a QMC cluster, of size  $L$ , into a much larger FLEX cluster of size  $L' \gg L$ , which is itself embedded in a mean-field. As we have shown here, this approach should be implemented by approximating the generating functional  $\Phi \approx \Phi_{QMC}(L) - \Phi_{FLEX}(L) + \Phi_{FLEX}(L')$ . Work along these lines is in progress.

We would like to acknowledge J.J. Deisz, D.W. Hess Th. Maier, S. Moukouri, and Th. Pruschke for very useful discussions and suggestions. This project was supported by NSF Grants No. DMR-0073308 and DMR-9704021.

179 (1977).

- [19] J. J. Deisz, D. W. Hess, and J. W. Serene, cond-mat/9411026R (To appear in "Recent Progress In Many Body Theories", vol. 4, edited by E. Schachinger, et al. (Plenum, New York)).
- [20] M. A. Jenkins, and J. F. Traub, Comm. ACM 15 (1972) 97-99. The routine is available at <http://www.netlib.org/tomspdf/419.pdf>.
- [21] Th. Maier, private communications.
- [22] A.A. Abrikosov, L.P. Gorkov and I.E. Dzyaloshinski, *Methods of Quantum Field Theory in Statistical Physics*, (Dover, New York, 1975).
- [23] T. Pruschke, private communications.

- 
- [1] T. Pruschke, M. Jarrell, and J. K. Freericks, Adv. Phys. **42**, 187 (1995).
  - [2] A. Georges, G. Kotliar, W. Krauth, and M. Rozenberg, Rev. Mod. Phys. **68**, 13 (1996).
  - [3] P. G. J. van Dongen, Phys. Rev. **B 50**, 14016 (1994).
  - [4] M. H. Hettler, M. Mukherjee, M. Jarrell, and H. R. Krishnamurthy, Phys. Rev. **B 61**, 12739 (2000).
  - [5] M. H. Hettler, A. N. Tahvildar-Zadeh, M. Jarrell, T. Pruschke, and H. R. Krishnamurthy, Phys. Rev. **B 58**, 7475 (1998).
  - [6] Th. A. Maier, M. Jarrell, Th. Pruschke, and J. Keller, Eur. Phys. J. **B 13**, 613-624 (2000).
  - [7] N. E. Bickers, D. J. Scalapino, and S. R. White, Phys. Rev. Lett. **62**, 961 (1989).
  - [8] N. E. Bickers, and S. R. White, Phys. Rev. **B 43**, 8044 (1990).
  - [9] J. J. Deisz, D. W. Hess, and J. W. Serene, Phys. Rev. Lett. **76**, 1312 (1996).
  - [10] J.W. Serene, and D. W. Hess, Phys. Rev. **B 44**, 3391 (1991).
  - [11] K. Aryanpour, M. H. Hettler, and M. Jarrell, Phys. Rev. **B 65**, 153102 (2002).
  - [12] Y. Imai, and N. Kawakami, preprint cond-mat/0204093.
  - [13] E. Müller-Hartmann, Z. Phys. **B 74**, 507-512 (1989).
  - [14] W. Metzner, and D. Vollhardt, Phys. Rev. Lett. **62**, 324 (1989).
  - [15] D.D. Betts, and G. E. Stewart, Can J. Phys. **v 75** n 1 (1997) p.47-66.
  - [16] G. Baym, Phys. Rev. **127**, 1391 (1962).
  - [17] Th. A. Maier, and M. Jarrell, Phys. Rev. **B 65**, 041104(R) (2002).
  - [18] H. J. Vidberg and J. W. Serene, J. Low Temp. Phys. **19**,